Magnetoplasmonic Triblock Nanorods for Collective Linear Dichroism

Jinxing Chen,[1,*] Ji Feng,[1] Panpan Xu,[1] and Yadong Yin[1, *]

[1] Department of Chemistry, University of California, Riverside, California 92521, United States

KEYWORDS: linear dichroism, plasmonic, polarization detection, confined growth

---

ABSTRACT: Polarized light detection is crucial for advancements in optical imaging, positioning, and obstacle avoidance systems. While optical nanomaterials sensitive to polarization are well-established, the ability to align these materials remains a significant challenge. Here, we introduce Au-Fe_3O_4-Au triblock nanorods as a novel solution. Synthesized via a space-confined seeded growth method, these magnetoplasmonic nanocomposites uniquely combine the strong polarization capabilities of Au nanorods with the magnetic alignment properties of Fe_3O_4 nanorods. This architecture results in exceptional collective linear dichroism, achieving a polarization ratio of approximately 14 at the device level. Our nanorods exhibit high detection sensitivity and laser damage resistance, positioning them as a promising platform for developing advanced optical devices.

INTRODUCTION

Linear dichroism refers to the difference in light extinction between polarizations parallel and perpendicular to a specific axis. It particularly exists in low-dimensional materials due to their strong anisotropy. Linear dichroic materials have applications in detecting polarized light, including near-field bioimaging, remote sensing, and communication.[1-5] For example, Sony is expanding its sensor technology leadership by introducing the on-chip polarization camera of Polarsens™, which, featuring an innovative 4-pixel block design with four unique angled polarizers, has brought polarized imaging to the next level.

The core of linear dichroic devices is the nanomaterial with polarized absorption, which is usually quantified by the extinction anisotropy along two perpendicular axes, i.e., linear dichroic ratio ($LCR = Ext_{0^o}/Ext_{90^o}$). For example, Wang et al. demonstrated linear dichroic photoluminescence of individual, isolated indium phosphide nanowires to define their potential optoelectronics.[2] Recently, Cui et al. showed a broadband photodetector using a layered black phosphorus transistor that is polarization-sensitive over a bandwidth from ~400 to 3750 nm.[3] The polarization sensitivity is due to the strong intrinsic linear dichroism arising from this material's in-plane optical anisotropy. Although much effort has been made to improve the LCR of individual nanostructures, a significant but often ignored point is that aligning them in devices is important because randomly distributed nanostructures hardly exhibit collective linear dichroism.[6, 7] As a typical example, a high LCR was found for isolated plasmonic Au nanorods, reaching hundreds of times the morphological aspect ratio. With their other advantageous features, such as high stability, tunable spectral region, low noise, and narrow plasmon bands, they are expected to find prominent applications in linear dichroism.[8-10] Unfortunately, this potential has not been fully demonstrated, mainly due to the difficulty of collective alignment.[6, 11-13] Therefore, optimizing collective LCR holds the key to the development of polarization devices.[14]

Here, we propose to develop Au-Fe_3O_4-Au triblock nanorods that couple magnetic and plasmonic components to achieve high collective LCR (inset in **Figure 1a**). This unique triblock nanorod structure integrates the strong polarization capability of two Au nanorods with the magnetic alignment capability of the center Fe_3O_4 nanorod, thereby activating the collective linear dichroism at the device level. Experimentally, we use space-confined seeded growth coupled with controlled seed ripening to prepare these triblock nanorods with tunable components and optical properties. Importantly, when these nanorods were encapsulated in a gel film, their orientation could be aligned well with an external magnetic field, thereby exhibiting a strong collective linear dichroism. The fabricated film demonstrated exceptional efficiency in detecting polarized light across varying power levels and sources, solidifying the potential of plasmonic nanostructures for polarization detection applications.

RESULTS AND DISCUSSION

Design of Au-Fe_3O_4-Au triblock nanorods

We first conducted the theoretical calculation of the extinction profiles to intuitively illustrate the linear dichroism of the triblock nanorods. Our model consists of an incident light propagating along the x axis and polarized along the y axis, and a triblock nanorod rotating in the xy plane (**Figure 1a**). The angle between the polarization direction of the light and the orientation of the triblock nanorod is defined as the polarization angle (θ). The triblock nanorod exhibits plasmonic resonance at ~540 nm and ~780 nm, corresponding to the transverse and longitudinal modes, respectively. As θ increases from 0° to 90°, the longitudinal plasmon mode gradually decreases, and the transverse mode becomes dominant. This trend is consistent with typical linear dichroic plasmonic nanorods (**Figure S1**). **Figure 1b** suggests that the extinction ability of the triblock nanorod at its resonant wavelength (~780 nm) has a clear angular dependence on the polarization angle. The relationship can be described as $I \propto I_0 \sin^2(2\theta)$, where I_0 is the intensity of incident polarized light, and θ is the polarization angle.[9]

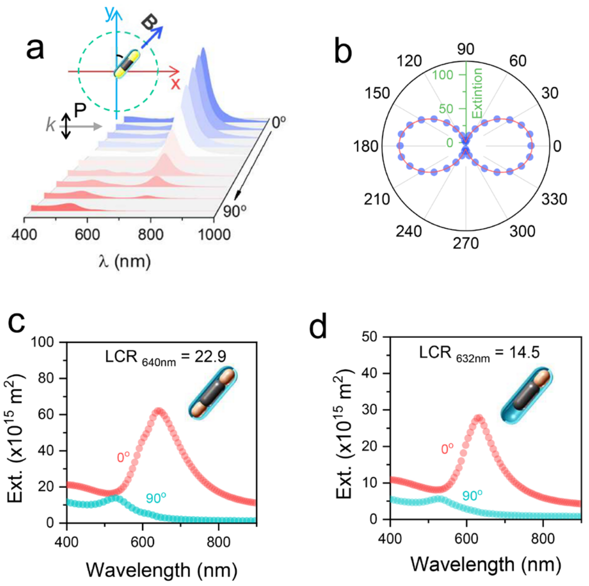

Figure 1. Linear dichroism of an Au-Fe_3O_4-Au triblock nanorod. ***a***, Simulated extinction of an Au-Fe_3O_4-Au triblock nanorod rotating from parallel direction (0°) to perpendicular direction (90°) with an angular interval of 10°. The dimensions of each Au are 85 nm in length and 40 nm in diameter, while the dimensions of Fe_3O_4 are 120 nm in length and 40 nm in diameter. ***b***, Polar plot of the extinction value of the longitudinal mode of the Au-Fe_3O_4-Au triblock nanorod as the function of the polarization angle. ***c***, ***d***, The extinction profiles and linear dichroic ratios of triblock (c) and diblock (d) nanorods.

We choose the triblock structure instead of the easily conceivable diblock ones because increasing the proportion of Au in a composite nanorod can enhance the final LCR value (**Figure 1c-1d**). The overall LCR value of a composite nanorod can be expressed as follows (see more details in **Figure S2**):

$$LCR_{comp.\ NR} = \chi + \frac{\sigma_{Fe}(\delta - \chi)}{\sigma_{Au} + \sigma_{Fe}} \qquad (1)$$

where σ_{Au} and σ_{Fe} are the extinction cross sections of Au and Fe_3O_4 nanorods perpendicular to incident light, respectively. χ and δ are the LCR of Au and Fe_3O_4 nanorods, respectively.

Since δ is smaller than χ, the LCR of composite nanorods is smaller than that of pure Au nanorods. In addition, the above equation can also be rewritten as Equation 2:

$$LCR_{comp.\ NR} = \chi + \frac{(\delta - \chi)}{1 + (\sigma_{Au}/\sigma_{Fe})} \qquad (2)$$

It suggests that a smaller component ratio of Fe_3O_4 increases the LCR of the nanocomposite. In short, the design of triblock nanorod is expected to offer two distinct benefits: (1) a larger absolute extinction cross-section area because of the doubled Au amount in each triblock nanorod; (2) a higher LCR by weakening the negative impact of Fe_3O_4.

Construction of Growth Templates

A space-confined seeded growth strategy was developed to construct the proposed Au-Fe_3O_4-Au triblock nanorods, as shown in **Figure 2a**. Specifically, uniform FeOOH nanorods with an average dimension of 200 × 42 nm (aspect ratio = 5, **Figure 2b**) were synthesized as the starting materials by direct hydrolysis of $FeCl_3 \cdot 6H_2O$ in an aqueous solution.[15] The surface of FeOOH nanorods was then functionalized with polyethyleneimine (PEI) as a bridge layer to load Au seeds (less than 3 nm) that were capped with tetrakis(hydroxymethyl)phosphonium chloride (**Figure 2c**).[16] The Au-loaded FeOOH nanorods were further modified with polyvinylpyrrolidone (PVP) and coated with a layer of resorcinol formaldehyde (RF) with an average thickness of 25 nm (FeOOH/Au@RF) (**Figure 2d**).

In order to create void spaces in the RF nanocapsules, we used a solution containing oxalic acid and PVP to partially etch the FeOOH nanorods from both ends. When oxalic acid was used alone, the etching reaction was too fast, leading to nonuniform products (**Figure S3**). Therefore, PVP was employed to slow the reaction, as it was suggested to complex with oxalic acid through hydrogen bonds and gradually release oxalic acid during its consumption.[17] As shown in **Figure 2e**, etching gradually shortened the

FeOOH nanorods, but there was no noticeable reduction in thickness.

An in-depth understanding of the relationship between etching conditions and morphological parameters helps the precise control of products. We thereby defined three parameters for quantitative analysis. The length (φ), width (δ) of the nanorods, and the gap size (γ) were measured from the TEM images and plotted against the etching time. In the initial etching stage with abundant PVP, the shortening of the FeOOH nanorods and the increase of the gap were relatively slow because the FeOOH nanorods were tightly wrapped by the RF nanoshell, making the contact between nanorods and etchants insufficient (**Figure 2f**). The etching rate increased once two gaps appeared at both ends, enabling more reaction opportunities between the oxalic acid and FeOOH. There was almost no change in the diameter of FeOOH nanorods during the entire etching process, suggesting a high etching selectivity. In addition, almost all the FeOOH nanorods were in the middle of the RF nanocapsules after etching, indicating equal etching rates on both ends. In contrast, if the etching process was performed with a low PVP concentration, we observed a more significant reduction in the width of the nanorods (**Figure 2f and S4**). Since the FeOOH nanorods have a polycrystalline structure, facet-selective etching is unlikely the mechanism (**Figure S5**). It is more reasonable to attribute the selective etching to a higher curvature of the nanorod tips rather than the sides.

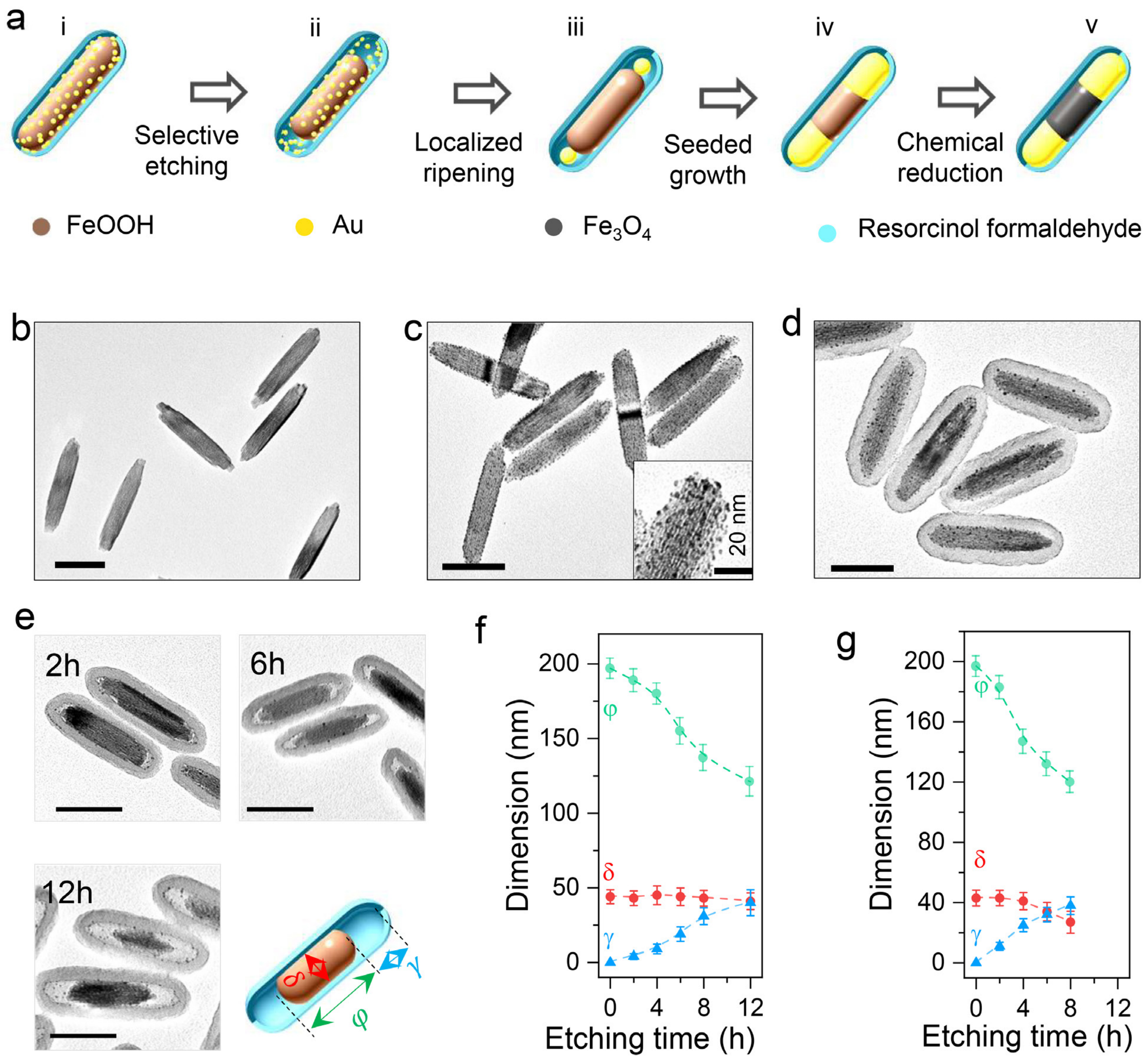

Figure 2. Growth of block nanorods in confined spaces. ***a***, Schematic illustration of the synthesis procedure of block nanorods, including i) synthesis of RF-coated FeOOH/Au nanorod (FeOOH/Au@RF), ii) selective etching of the FeOOH nanorod to generate uniform gaps, iii) ripening of seeds and iv) successive seeded growth, as well as v) converting FeOOH into Fe_3O_4. ***b***, ***c***, ***d***, TEM images of FeOOH (b), FeOOH/Au (c), and FeOOH/Au@RF (d) nanorods. Inset in Figure 2c is a magnified TEM image of

FeOOH/Au, where the dark dots are Au seeds. ***e***, Selective etching of FeOOH/Au@RF in an oxalic acid/PVP solution. ***f***, ***g***, Evolution of dimensions of FeOOH during etching processes: selective etching in the presence of abundant PVP, with a rapid decrease in length but unchanged diameter (f); low selectivity in the presence of insufficient PVP, with etching occurring at all directions (g). Scale bars are all 100nm.

Space-Confined Seeded Growth of Au-Fe_3O_4-Au Triblock Nanorods

We used a classic seeded growth process to deposit Au in the confined space, where PVP, ascorbic acid (AA), and chloroauric acid were added as the ligand, the reducing agent, and the precursor, respectively. Conventional seeded growth leads to equal opportunities for the growth of the Au seeds, resulting in the formation of multiple Au clusters (**Figure S6**). To avoid such an effect, we introduced potassium iodide (KI) to promote the ripening of small Au nanoparticles to two big ones at the ends of the nanorods (**Figure 3a**). KI was selected because it could work with oxygen to dissolve the tiny Au nanoparticles. The dissolved Au ions could be reduced by AA and deposited back onto the large Au nanoparticles, thereby minimizing the surface energy of the particles.[18, 19] As shown in **Figure S7**, the tiny Au seeds inside the RF shell disappeared, while some large Au nanoparticles appeared at both ends upon the introduction of KI.

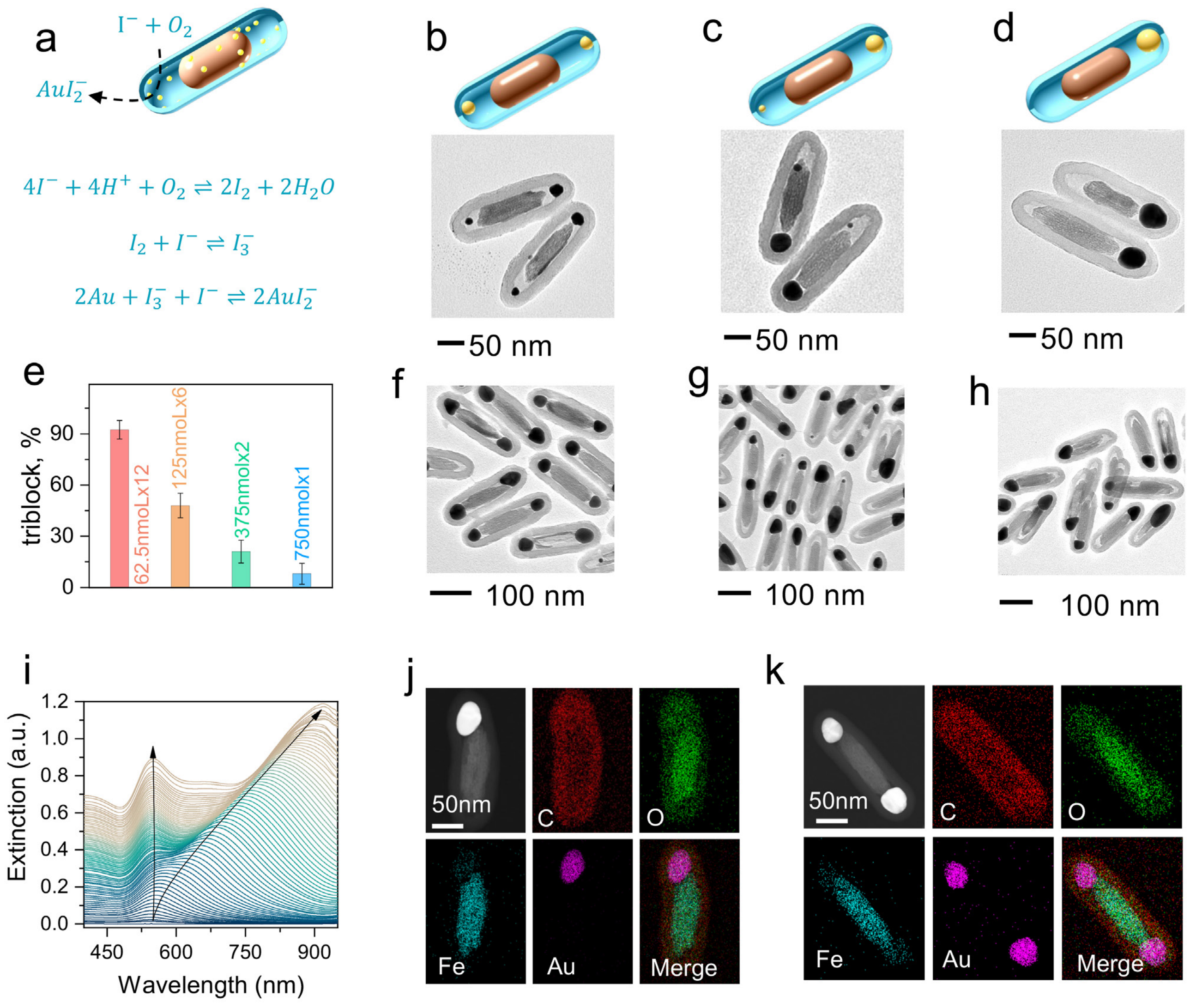

Figure 3. Ripening localization and seeded growth of Au within confined spaces. ***a***, Schematic illustration of the ripening of Au seeds promoted by KI. ***b***, ***c***, ***d***, Control over the localized ripening of Au seeds by tuning the injection rate of the precursor: a low injection rate induces a relatively weak ripening effect, producing two Au seeds within each RF capsule (b); increasing injection rate enhances the ripening process, forming two Au seeds of different sizes (c) or only one Au seed (d). ***e***, The effect of the injection rate of precursor on grown products. Increasing the injection rate reduces the yield of triblock nanorods. ***f***, ***g***, ***h***,

Products prepared by space-confined seeded growth method using the seeds shown in b, c, d. ***i***, In situ monitoring the seeded growth of triblock nanorods using UV-vis-NIR spectroscopy. ***j***, ***k***, STEM and elemental mapping images of Au-FeOOH-Au triblock nanorod (j), Au-FeOOH diblock nanorod (k).

The ripening of Au nanoparticles has to be precisely controlled to achieve equal Au nanorods at both ends of the RF capsule. In order to show the importance of kinetics control to the morphology of the final product, we kept the concentration of KI constant and adjusted the growth kinetics by varying the injection rate of the Au precursor. In our reaction system, the concentration of KI was much larger than that of Au, which ensured that Au was the limiting reagent in the ripening process. As shown in **Figure 3b**, when the injection rate of the precursor was slowed down to 62.5 nmol per injection with a time interval of 2 min, two Au nanoparticles were formed at both ends of the nanorod. Increasing the injection rate to 200 nmol per injection caused uneven ripening, so two Au nanoparticles of different sizes appeared in the gaps (**Figure 3c**). Further increasing the injection rate to 750 nmol per injection produced only one big Au seed inside the RF capsule (**Figure 3d**). These results suggest that a slow ripening process is more conducive to the formation of two Au nanoparticles. In addition, the morphology of the final product is also determined by the gap size. For example, a single Au nanoparticle was observed in a large gap, and incomplete ripening occurred in a small gap (**Figure S8**). Benefiting from the localized ripening effect, we have controllably locked one or two Au seeds within the nanocapsules. As an important feature of template-based approaches, our process offers the advantage of scalability, as the templates can be obtained on a large scale and at a low cost through simple reactions. In addition, as shown in **Figure 3e-3h**, the uniform Au-FeOOH diblock or Au-FeOOH-Au triblock nanorods could be prepared with high yields. For example, with a low injection rate of precursor, the yield of Au-FeOOH-Au triblock nanorod attained ~90% (**Figure 3e, S9**).

The evolution of triblock nanorods during the synthesis was in situ monitored by UV-vis-NIR spectroscopy, as shown in **Figure 3i**. At the early stage of the reaction, as the size of the gold increased, and the extinction peak gradually broadened and shifted to longer wavelengths. When the reaction progressed to about 1200 seconds, the original absorption peak split into two peaks at around 540 nm and 610 nm, which were attributed to the transverse and longitudinal modes of Au nanorod. After that, the wavelength of the transverse mode did not change much, and the longitudinal mode continuously shifted to about 780 nm.

The composition of the triblock and diblock nanorods was characterized by high-angle annular dark-field scanning transmission electron microscopy (HAADF-STEM) imaging and elemental mapping. As shown in **Figures 3j and 3k**, Au is distributed at one or two ends of Fe, and there is no overlapping between the two elements, proving the well-controlled ripening and seeded growth reactions. Furthermore, Ag has also been successfully deposited into the nanocomposites to form Au@Ag-FeOOH diblock nanorods or Au-FeOOH-Ag triblock nanorods, showcasing the flexibility and robustness of the synthesis (**Figure S10, S11**).

Magnetic Field-Controlled Extinction Anisotropy

In order to achieve orientational control of the nanocomposites, the FeOOH nanorods were reduced with hydrazine to the magnetic Fe_3O_4 counterparts. The overall morphology was well-maintained during the transformation process due to the RF protection (**Figure S12**). **Figure 4a** shows the hysteresis-loop of the triblock nanorods measured at room temperature. The magnetization curves saturated at a low magnetic field, suggesting they could quickly respond to the external magnetic field. The plasmonic extinction of the triblock nanorods changes with alternating the direction of the magnetic field. As shown in **Figure 4b**, when the triblock nanorods were parallel to the polarization direction of the incident light (0°), the longitudinal mode (~650 nm) of the nanorods was excited. As the angle between the nanorods and the polarization direction increased, the transverse mode was gradually excited, and the longitudinal mode retired to a dark mode. An obvious dichroism is shown in **Figure 4c**. When the orientation of the nanocomposites was rotated from perpendicular to the magnetic field direction to parallel to the magnetic field direction, the color of the suspension changed significantly from red to green. The magnetic switching of the two resonant modes was very fast and reversible, as confirmed by the continuous optical switching in an alternating magnetic field of 0.6 Hz and ~2.3 Hz (**Figure 4d**).

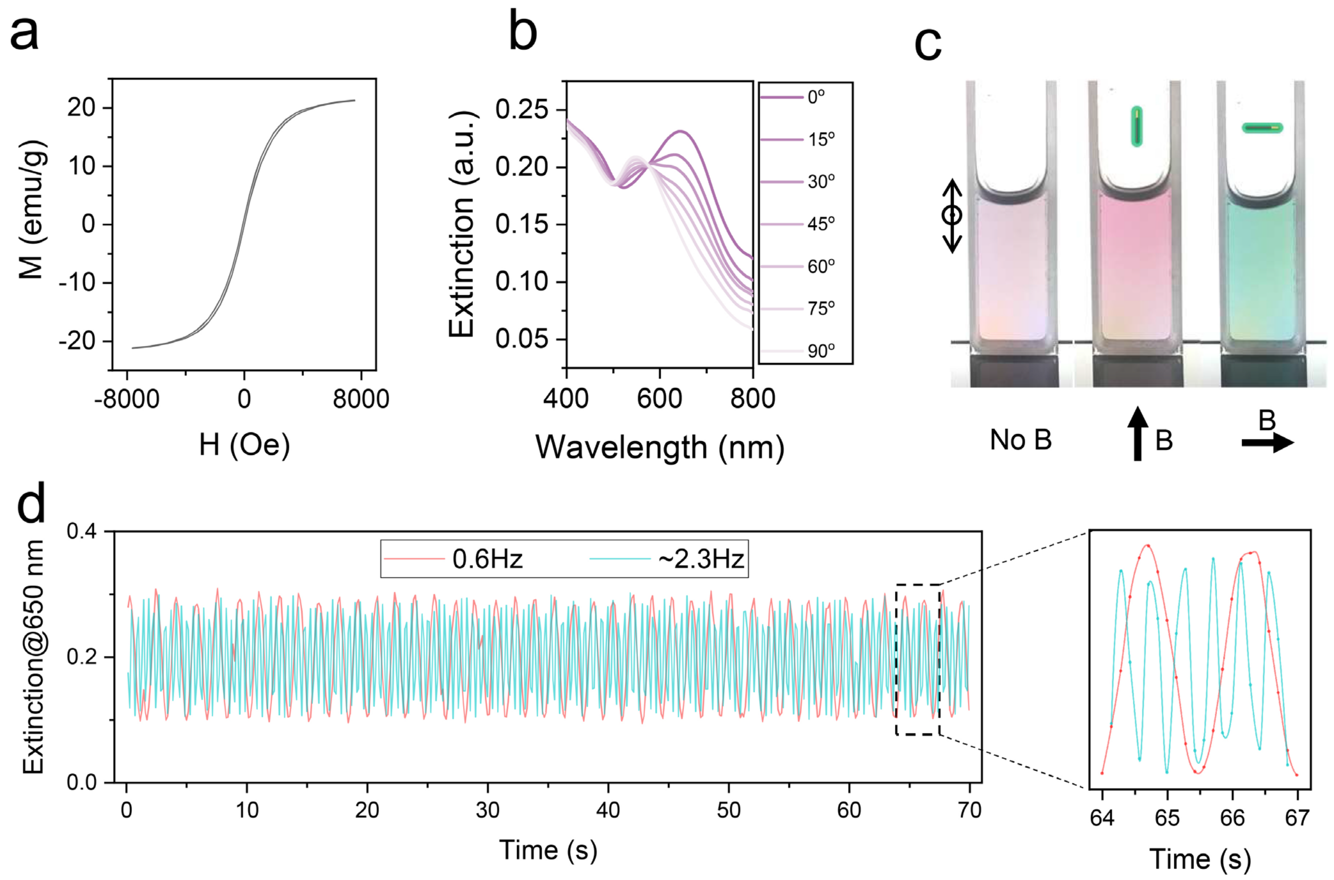

Figure 4. Magnetically induced optical switching of triblock nanorods. ***a***, Magnetic hysteresis loop of triblock nanorods. ***b***, Extinction profiles of triblock nanorods with different orientations. ***c***, Change of transmitted color of the nanorod dispersion in response to a magnetic field. ***d***, Dynamic switching of extinction intensity at a resonant wavelength of 650 nm using an alternating magnetic field.

We also prepared magnetic Au-Fe_3O_4 diblock nanorods, investigated their polarization ability, and proved the advantages of the Au-Fe_3O_4-Au triblock nanorods over the Au-Fe_3O_4 diblock nanorods by comparing their LCR values. Although the plasmonic extinction of the diblock nanorods also showed excellent linear dichroism characteristics (**Figure S13**), their LCR is significantly smaller than that of the corresponding triblock nanorods (**Figure S14**), because each triblock nanorod contains a double amount of Au compared to the diblock one. Besides, the triblock nanorods also have a much higher linear dichroism property, which is consistent with our theoretical analysis.

Detection of Polarized Light

The large LCR and the convenient magnetic orientational control make the Au-FeOOH-Au triblock nanorods useful for polarized light detection. To fit the scenario of real application, the nanocomposites were embedded in a transparent matrix and made into a solid film. Specifically, the nanorods mixed with the hydrogel precursors were injected into a mold. A composite hydrogel with well-aligned block nanorods was prepared by applying an external magnetic field followed by subsequent exposure to ultraviolet light (**Figure S15**).

To systematically investigate the polarization properties of the composite film, we prepared four batches of triblock nanorods with longitudinal modes at different wavelengths (645 nm, 692 nm, 730 nm, and 810 nm) and aligned them in solid films (TB645, TB692, TB730, and TB810). The total number of nanocomposites in each film was kept the same. Our optical setup is shown in **Figure 5a**. To match the resonant peak of the longitudinal plasmonic excitation for each sample, we chose lasers with wavelengths of 647, 692, 734, and 806 nm as the incident beam. The samples were fixed on a rotation plate to control their relative orientation with respect to the polarization direction of the laser. A power meter was used to measure the intensity of direct transmission through the sample. As shown in **Figure 5b**, the four films exhibit angle-dependent extinction with rotation periods of 180°, indicating excellent linear dichroism characteristics. The polarization ability was calculated by dividing the maximum extinction value of the composite film by the minimum value (PR = I_{max} / I_{min}) and the result is shown in **Figure 5c**.[20] The PR value increases as the resonant peak moves to longer wavelengths, which is consistent with our simulation results (**Figure S1**). It is worth noting that the PR of the nanocomposite film is up to ~14 for TB810, which is much higher than its geometrical aspect ratio. This PR value is also higher than those previously reported polarized light devices based on 1D nanorods, such as $CsPbBr/I_3$ nanowire (~2.6), CdSe nanorod (~1.2), and anisotropic 2D materials, such as GeAs2 (~2), GeSe (~3). The experimentally determined PRs of some reported polarized light photodetectors are summarized in **Figure 5d**.[2, 4, 20-26] It is worth pointing out that the detection of near-infrared polarized light is more promising, especially in the biological field, such as infrared polarized light imaging and laser calibration.[27, 28]

The polarization angle of the incident beam was determined by measuring three sets of direct transmission intensities and solving the Mueller matrix. The polarization state of electromagnetic radiation can be described by the Stokes vector (S):

$$S = [I, Q, U, V]^T, \tag{3}$$

where I is the polarized light intensity, Q is the linearly polarized horizontal component, U is the linearly polarized 45° component, and V is the right-handed circularly polarized light component. When the incident polarized light passes through a linear polarizer, the Stokes vector of the transmitted light can be expressed as:

$$S' = \begin{bmatrix} I' \\ Q' \\ U' \\ V' \end{bmatrix} = M(\theta_p) \times S =$$

$$\frac{1}{2}\begin{bmatrix} 1 & cos2\theta_p & sin2\theta_p & 0 \\ cos2\theta_p & cos^2 2\theta_p & cos2\theta_p \cdot sin2\theta_p & 0 \\ sin2\theta_p & cos2\theta_p \cdot sin2\theta_p & sin^2 2\theta_p & 0 \\ 0 & 0 & 0 & 0 \end{bmatrix}\begin{bmatrix} I \\ Q \\ U \\ V \end{bmatrix} \tag{4}$$

where $M(\theta_p)$ is the Mueller matrix, θ_p the angle between the polarization direction of the light and that of the polarizer. The power of the transmitted light can be expressed as:

$$I'(\theta_p) = \frac{1}{2}\left(I + Q \cdot cos2\theta_p + U \cdot sin2\theta_p\right) \tag{5}$$

Although the I, Q, U are unknown, they can be solved by measuring the intensity of the transmitted light in any three directions. For the convenience of calculation, we set the sequence angles as 0°, 60°, and 120°, respectively. The Stokes parameter of the transmitted light can be simplified as follows:

$$\begin{cases} I = \frac{2}{3}[I'(0) + I'(60) + I'(120)] \\ Q = \frac{2}{3}[2I'(0) - I'(60) - I'(120)] \\ U = \frac{2}{\sqrt{3}}[I'(60) - I'(120)] \end{cases} \tag{6}$$

In addition, the polarization degree and polarization angle of incident light can also be solved after deriving Equations 5 and 6.

$$P = \frac{\sqrt{Q^2+U^2+V^2}}{I} \approx \frac{\sqrt{Q^2+U^2}}{I} \tag{7}$$

$$\theta_p = \frac{1}{2}\arctan\left(U/Q\right) \tag{8}$$

To evaluate the detection performance of our film, we prepared three TB810 films with orientation angles of 0°, 60°, and 120° and assembled them into a chip card (upper image in **Figure 5e**). The simple detection setup only requires the chip card and a power meter aligned along the incident light (**Figure 5e**, bottom image). When the film was tested with an 806 nm laser of different linear polarization directions (1.20°, 24.0°, -32.0°, -18.0°), it exhibited high detection precisions. Figure 5f shows the transmission intensity of the light through the three differently oriented TB810 films and the calculated polarization angles. The polarization angle was calculated to be -1.25°, 24.4°, -31.7°, and -17.6°. Further, we also show that polarization detection can be operated in a wide dynamic range (**Figure 5g, S16a**). We want to emphasize that the effective power density was calculated to be in the range of 0.05 to 1.5 W/cm², the typical power window used in many biomedical applications.[29, 30] Compared with a simple commercial polarizer, our linear polarized light detection system offers a significantly larger PR than the commercial polarizer (**Figure S16b**). Also, the commercial polarizer has very poor resistance to laser heating, losing its polarization function due to the photothermal destruction when the incident power is above 25 mW. In contrast, TB810 exhibited excellent resistance to high-power incident light, likely due to the high thermal stability of Au nanoparticles and their strong light-scattering capability (**Figure S17**), which collectively enhance overall stability. Our chip card exhibited excellent cycling performance (**Figure S18**).

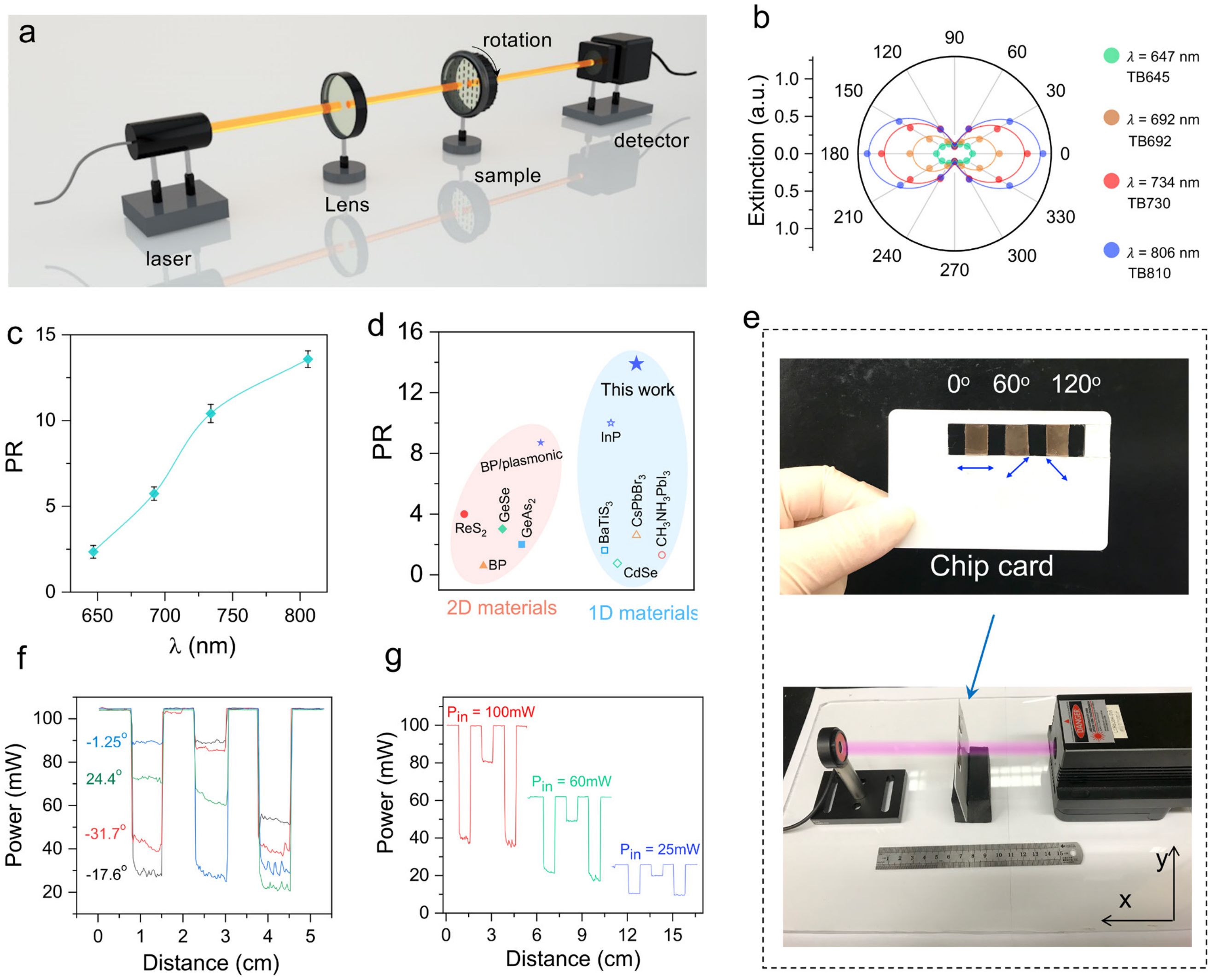

Figure 5. Detection of polarized light. ***a***, Schematic illustration of a homemade device for the detection of angular dependent extinction ability of films. ***b***, Polar plot of the angular-resolved extinction of various triblock nanorod films. ***c***, Summarized LCR of triblock nanorod films at their resonant wavelengths. ***d***, Experimental LCR of some reported polarized light detectors. ***e***, Upper image: a fabricated chip card consisting of three columns of films with aligned orientations of 0°, 60°, and 120°. Bottom image: the homemade polarized light detection system including a laser, a sample stage, and a photodiode. ***f***, Different power readings of the chip card when measured under the illumination of linearly polarized light with different polarization angles. ***g***, Different power readings of the chip card when measured under the illumination of linearly polarized light with fixed polarization angles but different incident powers.

CONCLUSION

We have successfully developed magnetoplasmonic triblock nanorods that could be magnetically aligned to achieve collective linear dichroism for high-performance polarized light detection. These triblock nanorods, each consisting of two Au nanorods linearly attached to the two ends of a Fe_3O_4 nanorod, were synthesized through a space-confined seeded growth strategy. By embedding these nanorods with collective magnetic alignment in a hydrogel, we further produced linear dichroic composite films that demonstrated outstanding performance in polarized light detection. Featuring high detection sensitivity and laser damage resistance, the magnetically actuated linear dichroic Au nanorods offer a versatile platform for constructing advanced optical devices with broad applications in bioimaging, optical modulation, and stress sensing.

ASSOCIATED CONTENT

Supporting Information

The Supporting Information is available free of charge on the ACS Publications website.

Experimental Section, Theoretical calculation of linear dichroism ratio, Morphologies of samples, Polarization ability of block nanorods, Polarization detection

AUTHOR INFORMATION

Corresponding Author

* Jinxing Chen, chenjinxing@suda.edu.cn
* Yadong Yin, yadong.yin@ucr.edu

Author Contributions

The manuscript was written with contributions from all authors.

Notes

The authors declare no competing financial interest.

ACKNOWLEDGMENT

The authors are grateful for the financial support from the U.S. National Science Foundation (CHE- 2203972).

REFERENCES

1. Bailey, J.; Sparks, W. B.; Hough, J. H.; Axon, D. J., Infrared polarimetry of the nucleus of Centaurus A: the nearest blazar? *Nature* **1986,** *322* (6075), 150-151.
2. Wang, J.; Gudiksen, M. S.; Duan, X.; Cui, Y.; Lieber, C. M., Highly polarized photoluminescence and photodetection from single indium phosphide nanowires. *Science* **2001,** *293* (5534), 1455-7145.
3. Yuan, H.; Liu, X.; Afshinmanesh, F.; Li, W.; Xu, G.; Sun, J.; Lian, B.; Curto, A. G.; Ye, G.; Hikita, Y.; Shen, Z.; Zhang, S. C.; Chen, X.; Brongersma, M.; Hwang, H. Y.; Cui, Y., Polarization-sensitive broadband photodetector using a black phosphorus vertical p-n junction. *Nat Nanotechnol* **2015,** *10* (8), 707-713.
4. Wang, X.; Li, Y.; Huang, L.; Jiang, X. W.; Jiang, L.; Dong, H.; Wei, Z.; Li, J.; Hu, W., Short-Wave Near-Infrared Linear Dichroism of Two-Dimensional Germanium Selenide. *J Am Chem Soc* **2017,** *139* (42), 14976-14982.
5. Peng, Y.; Liu, X.; Sun, Z.; Ji, C.; Li, L.; Wu, Z.; Wang, S.; Yao, Y.; Hong, M.; Luo, J., Exploiting the Bulk Photovoltaic Effect in a 2D Trilayered Hybrid Ferroelectric for Highly Sensitive Polarized Light Detection. *Angew Chem Int Ed* **2020**, *59* (10), 3933-3937.
6. Cubukcu, E.; Degirmenci, F.; Kocabas, C.; Zimmler, M. A.; Rogers, J. A.; Capasso, F., Aligned carbon nanotubes as polarization-sensitive, molecular near-field detectors. *Proc Natl Acad Sci U S A* **2009,** *106* (8), 2495-2499.
7. Ming, T.; Zhao, L.; Yang, Z.; Chen, H.; Sun, L.; Wang, J.; Yan, C., Strong polarization dependence of plasmon-enhanced fluorescence on single gold nanorods. *Nano Lett* **2009,** *9* (11), 3896-3903.
8. Sonnichsen, C.; Alivisatos, A. P., Gold nanorods as novel nonbleaching plasmon-based orientation sensors for polarized single-particle microscopy. *Nano Lett* **2005,** *5* (2), 301-304.
9. Wang, M.; Gao, C.; He, L.; Lu, Q.; Zhang, J.; Tang, C.; Zorba, S.; Yin, Y., Magnetic tuning of plasmonic excitation of gold nanorods. *J Am Chem Soc* **2013,** *135* (41), 15302-15305.
10. Hadar, I.; Hitin, G. B.; Sitt, A.; Faust, A.; Banin, U., Polarization Properties of Semiconductor Nanorod Heterostructures: From Single Particles to the Ensemble. *J Phys Chem Lett* **2013,** *4* (3), 502-507.
11. Liu, S.; Li, J.; Li, Z.-Y., Macroscopic Polarized Emission from Aligned Hybrid Gold Nanorods Embedded in a Polyvinyl Alcohol Film. *Adv Opt Mater* **2013,** *1* (3), 227-231.
12. Ren, Y. X.; Kelly, T. S.; Zhang, C.; Xu, H.; Chen, Z., Soliton-mediated orientational ordering of gold nanorods and birefringence in plasmonic suspensions. *Opt Lett* **2017,** *42* (3), 627-630.
13. Chang, W. S.; Ha, J. W.; Slaughter, L. S.; Link, S., Plasmonic nanorod absorbers as orientation sensors. *Proc Natl Acad Sci U S A* **2010,** *107* (7), 2781-2786.
14. Fang, Y.; Dong, Q.; Shao, Y.; Yuan, Y.; Huang, J., Highly narrowband perovskite single-crystal photodetectors enabled by surface-charge recombination. *Nat Photonics* **2015,** *9* (10), 679-686.
15. Chen, J.; Feng, J.; Yang, F.; Aleisa, R.; Zhang, Q.; Yin, Y., Space-Confined Seeded Growth of Cu Nanorods with Strong Surface Plasmon Resonance for Photothermal Actuation. *Angew Chem Int Ed* **2019,** *58* (27), 9275-9281.
16. Chen, J.; Feng, J.; Li, Z.; Xu, P.; Wang, X.; Yin, W.; Wang, M.; Ge, X.; Yin, Y., Space-Confined Seeded Growth of Black Silver Nanostructures for Solar Steam Generation. *Nano Lett* **2019,** *19* (1), 400-407.
17. Chen, H.; Colvin, D. C.; Qi, B.; Moore, T.; He, J.; Mefford, O. T.; Alexis, F.; Gore, J. C.; Anker, J. N., Magnetic and optical properties of multifunctional core-shell radioluminescence nanoparticles. *J Mater Chem* **2012,** *22* (25), 12802-12809.
18. Feng, J.; Xu, D.; Yang, F.; Chen, J.; Wu, C.; Yin, Y., Surface Engineering and Controlled Ripening for Seed-Mediated Growth of Au Islands on Au Nanocrystals. *Angew Chem Int Ed* **2021,** *60* (31), 16958-16964.
19. Li, Z.; Zhang, J.; Jin, J.; Yang, F.; Aleisa, R.; Yin, Y., Creation and Reconstruction of Thermochromic Au Nanorods with Surface Concavity. *J Am Chem Soc* **2021,** *143* (38), 15791-15799.
20. Wu, J.; Cong, X.; Niu, S.; Liu, F.; Zhao, H.; Du, Z.; Ravichandran, J.; Tan, P. H.; Wang, H., Linear Dichroism Conversion in Quasi-1D Perovskite Chalcogenide. *Adv Mater* **2019,** *31* (33), e1902118.
21. Singh, A.; Li, X.; Protasenko, V.; Galantai, G.; Kuno, M.; Xing, H. G.; Jena, D., Polarization-sensitive nanowire photodetectors based on solution-synthesized CdSe quantum-wire solids. *Nano Lett* **2007,** *7* (10), 2999-3006.
22. Zhu, P.; Gu, S.; Shen, X.; Xu, N.; Tan, Y.; Zhuang, S.; Deng, Y.; Lu, Z.; Wang, Z.; Zhu, J., Direct Conversion of Perovskite Thin Films into Nanowires

with Kinetic Control for Flexible Optoelectronic Devices. *Nano Lett* **2016,** *16* (2), 871-876.

23. Liu, F.; Zheng, S.; He, X.; Chaturvedi, A.; He, J.; Chow, W. L.; Mion, T. R.; Wang, X.; Zhou, J.; Fu, Q.; Fan, H. J.; Tay, B. K.; Song, L.; He, R.-H.; Kloc, C.; Ajayan, P. M.; Liu, Z., Highly Sensitive Detection of Polarized Light Using Anisotropic 2D ReS2. *Adv Funct Mater* **2016,** *26* (8), 1169-1177.

24. Li, L.; Gong, P.; Sheng, D.; Wang, S.; Wang, W.; Zhu, X.; Shi, X.; Wang, F.; Han, W.; Yang, S.; Liu, K.; Li, H.; Zhai, T., Highly In-Plane Anisotropic 2D GeAs2 for Polarization-Sensitive Photodetection. *Adv Mater* **2018,** *30* (50), e1804541.

25. Zhao, S.; Wu, J.; Jin, K.; Ding, H.; Li, T.; Wu, C.; Pan, N.; Wang, X., Highly Polarized and Fast Photoresponse of Black Phosphorus-InSe Vertical p-n Heterojunctions. *Adv Funct Mater* **2018,** *28* (34), 1802011.

26. Wu, D.; Guo, J.; Du, J.; Xia, C.; Zeng, L.; Tian, Y.; Shi, Z.; Tian, Y.; Li, X. J.; Tsang, Y. H.; Jie, J., Highly Polarization-Sensitive, Broadband, Self-Powered Photodetector Based on Graphene/PdSe2/Germanium Heterojunction. *ACS Nano* **2019,** *13* (9), 9907-9917.

27. Li, D.; He, H.; Zeng, N. A. N.; Du, E.; Liao, R. A. N.; He, Y.; Ma, H. U. I.; Liu, S.; Li, M., Polarization Imaging and Scattering Model of Cancerous Liver Tissues. *J Innov Opt Health Sci* **2013,** *06* (3), 1350025.

28. Lin, H.; Gao, S.; Dai, C.; Chen, Y.; Shi, J., A Two-Dimensional Biodegradable Niobium Carbide (MXene) for Photothermal Tumor Eradication in NIR-I and NIR-II Biowindows. *J Am Chem Soc* **2017,** *139* (45), 16235-16247.

29. Chen, J.; Lei, S.; Xie, Y.; Wang, M.; Yang, J.; Ge, X., Fabrication of High-Performance Magnetic Lysozyme-Imprinted Microsphere and Its NIR-Responsive Controlled Release Property. *ACS Appl Mater Interfaces* **2015,** *7* (51), 28606-28615.

30. Chen, J.; Lei, S.; Zeng, K.; Wang, M.; Asif, A.; Ge, X., Catalase-imprinted Fe3O4/Fe@fibrous SiO2/polydopamine nanoparticles: An integrated nanoplatform of magnetic targeting, magnetic resonance imaging, and dual-mode cancer therapy. *Nano Research* **2017,** *10* (7), 2351-2363.

TOC